C. R. Mecanique 344 (2016) 211–224

Contents lists available at ScienceDirect

Comptes Rendus Mecanique

www.sciencedirect.com

Computational simulation of manufacturing processes

SPH modeling of adhesion in fast dynamics: Application to the Cold Spray process

Paul Profizi [a,c], Alain Combescure [a,b,*], Kahuziro Ogawa [c]

[a] LaMCoS UMR 5259, INSA LYON, 18-20 Allée des sciences, 69621 Villeurbanne, France
[b] AREVA–SAFRAN chair, France
[c] Fracture and Reliability Research Institute, Tohoku University, 6-6-1, Aramaki, Aoba-ku, Sendai, 980-8573, Miyagi, Japan

ARTICLE INFO

Article history:
Received 17 September 2015
Accepted after revision 15 November 2015
Available online 8 February 2016

Keywords:
Adhesive forces
Modeling
Smooth particle hydrodynamics
Cold Spray
Fast dynamics

ABSTRACT

The objective of this paper is to show, in a specific case, the importance of modeling adhesive forces when simulating the bouncing of very small particles impacting a substrate at high speed. The implementation of this model into a fast-dynamics SPH code is described. Taking the example of an impacted elastic cylinder, we show that the adhesive forces, which are surface forces, play a significant role only if the particles are sufficiently small. The effect of the choice of the type of interaction law in the cohesive zone is studied and some conclusions on the relevance of the modeling of the adhesive forces for fast-dynamics impacts are drawn. Then, the adhesion model is used to simulate the Cold Spray process. An aluminum particle is projected against a substrate made of the same material at a velocity ranging from 200 to 1000 $m{\cdot}s^{-1}$. We study the effects of the various modeling assumptions on the final result: bouncing or sticking. Increasingly complex models are considered. At a 200 $m{\cdot}s^{-1}$ impact velocity, elastic behavior is assumed, the substrate being simply supported at its base and supplied with absorbing boundaries. The same absorbing boundaries are also used for all the other simulations. Then, plasticity is introduced and the impact velocity is increased up to 1000 $m{\cdot}s^{-1}$. At the highest velocities, the resulting strains are very significant. The calculations show that if the adhesion model is appropriately chosen, it is possible to reproduce the experimental observations: the particles stick to the substrate in a range of impact velocities surrounded by two velocity ranges in which the particles bounce.

1. Introduction

We are going to study the modeling of the Cold Spray process, which consists in coating an object with a thin layer of a metallic or amorphous material by projecting very small particles at high speed. Historically, the process was first developed only experimentally [1]. These experiments showed that these coatings adhere only for certain pairs of materials and within a specific velocity range [2]. Furthermore, if the particles are too large, sticking no longer occurs. Many hypotheses, such as the presence of a shear strip at the interface upon impact, have been formulated to explain these experimental obser-

* Corresponding author at: Laboratoire de mécanique des contacts et des structures, INSA de Lyon, UMR CNRS 5259, 18–20, rue des Sciences, 69621 Villeurbanne, France. Tel.: +33 (0)4 72 43 64 26; fax: +33 (0)4 78 89 09 80.
E-mail address: alain.combescure@insa-lyon.fr (A. Combescure).

http://dx.doi.org/10.1016/j.crme.2016.02.001

vations [3]. They were based on the subsequent observation of the microstructures and their association with numerical results giving the histories of temperatures and other parameters at the interface [4]. These numerical results relied mainly on explicit dynamic finite element calculations [5]. However, most finite element calculations are unable to simulate the very significant crushing of soft particles against a rigid substrate or the deep penetration of hard particles into a softer substrate, so they often resort to a remeshing method [4]. Some calculations are based on coupled Euler/Lagrange formulations: these lead to better results when one of the two objects is subjected to very high strains [6]. Solid SPH methods also appear to lead to good predictions in the case of highly distorted meshes. They also enable local material tearing to be easily simulated [7–10]. Adhesive forces become significant when the size of the objects in contact becomes very small. Today, only very few finite element or SPH fast dynamics numerical simulation tools take into account adhesive forces during impact [11]. One thesis [7] implemented them within an SPH model, but the method is relatively crude. The purpose of this paper is to show what types of models can be chosen for adhesion and how they can be implemented within a solid SPH framework.

Thus, the first section describes how these adhesive forces can be represented in a solid SPH model and presents the various adhesion models available.

The second section deals with a very simple example which consists in predicting the elastic rebound of a cylinder projected at 20 $\mathrm{m\,s^{-1}}$ against another cylinder of twice its diameter which is built-in at its base. Before that, the effects of taking into account the adhesion phenomenon and the specimen's size on the rebound are evaluated.

The third section studies the case of the impact of a sphere onto a plane. First, the effects of the parameters of the adhesion law and of the presence of absorbing boundaries are presented for a purely elastic impact case. Then, an elastic–plastic material model of the Johnson–Cook type taking into account adiabatic heating is introduced. The effects of the impact velocity and of the adhesion model and parameters are presented.

2. Modeling

All the numerical simulations developed in this work are based on an explicit dynamic approach. The integration scheme is a Newmark scheme ($\beta = 0, \alpha = 0.5$). After a review of the SPH method applied to solids and of the constitutive relations used in this application, we will undertake to develop more specifically the contact approach chosen in this publication. The pinball technique and Lagrange multipliers are used respectively to detect contacts and to calculate the contact load. Finally, we will show how the adhesion models can be easily implemented in this context.

2.1. Review of the SPH method

The SPH method has been known for many years and used for the development of many physical models with very different topologies. This type of method is a meshless approach which involves only nodes (the SPH points). The strains at each point are calculated from the displacement field of all the points located in a sphere B of radius h centered on the point (h being, of course, greater than the standard distance between two points). Any function $f(\mathbf{x})$ of the coordinate $\mathbf{x}$ is represented by the following integral:

$$f(\mathbf{x}) \simeq \int_B f(\mathbf{x}')W((\mathbf{x}-\mathbf{x}'),h)\,\mathrm{d}\mathbf{x}' \tag{1}$$

in which $W(\mathbf{x},h)$ is the kernel function which imitates the Dirac function (δ). In order to guarantee a consistent solution, W must possess the following properties:

- normalization

$$\int_B W((\mathbf{x}-\mathbf{x}'),h)\,\mathrm{d}\mathbf{x}' = 1 \tag{2}$$

- symmetry

$$W((\mathbf{x}-\mathbf{x}'),h) = W((\mathbf{x}'-\mathbf{x}),h)\nabla[W((\mathbf{x}-\mathbf{x}'),h)] = \nabla[W((\mathbf{x}'-\mathbf{x}),h)] \tag{3}$$

- Dirac limit

$$\lim_{h\to 0} W((\mathbf{x}-\mathbf{x}'),h) = \delta(\mathbf{x}-\mathbf{x}') \tag{4}$$

- Compact support

$$W((\mathbf{x}),h) = 1\ h > \kappa h \tag{5}$$

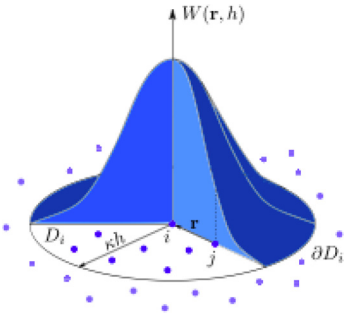

Fig. 1. The kernel function W.

A typical kernel function is shown in Fig. 1. The equation chosen to represent this function is:

$$w(r_{ij},h)=C\begin{cases}\frac{3}{2}\left[\frac{2}{3}-\left(\frac{r_{ij}}{h}\right)^2+\frac{1}{2}\left(\frac{r_{ij}}{h}\right)^3\right] & \text{if } 0\le\frac{r_{ij}}{h}\le 1\\ \frac{1}{4}\left[2-\frac{r_{ij}}{h}\right]^3 & \text{if } 1<\frac{r_{ij}}{h}<2\\ 0 \text{ otherwise}\end{cases} \tag{6}$$

with $r_{ij}=\|\mathbf{x_i}-\mathbf{x_j}\|$ and $C=1/\pi h^3$ in 3D. Let us consider SPH node i and approximate the integral in Eq. (1) numerically using the quadrature formula of Eq. (7):

$$f(\mathbf{x_i})=\Sigma_{j\in B_i} f(\mathbf{x_j})W(\mathbf{x_i}-\mathbf{x_j})\omega_j \tag{7}$$

In Eq. (7), B_i is the sphere of radius $h=\kappa h$ centered on i, whereas j is a node belonging to this sphere. Point j is associated with an elementary volume ω_j. The gradients of a function are approximated in a similar way:

$$\nabla f(\mathbf{x_i})=\Sigma_{j\in B_i} f(\mathbf{x_j})\nabla W(\mathbf{x_i}-\mathbf{x_j})\omega_j \tag{8}$$

This type of formulation was first developed for the simulation of large displacements of fluids and gases [12]. The material models, in general, had no memory effects and all the physical models studied were highly dissipative. The first applications to solids showed that the previous formalism led to artificial fracture mechanisms, even in the case of a linear elastic material with no damage model. This defect, known as tensile instability, was corrected [13] by introducing an appropriate renormalization of the kernel functions, a total Lagrangian formulation of the solid mechanics equations and some artificial viscosity. In addition, a series of auxiliary points (stress points, positioned like Gauss points) helps eliminate the hourglass modes which can appear in some cases. When one chooses this type of implementation, the SPH nodes are associated with the kinematic variables while the stress points are associated with the static variables (along with the associated history variables). We will not give any further details on the formulation, which can be found, e.g., in [14,15] for volume formulations and in [16,17] for shell formulations. In this paper, we chose the initial normalized 3D formulation (without stress points). This choice is justified by the existence of very large plastic strains which occur in the simulations, which dissipate enough energy to prevent hourglass modes from developing.

2.2. Modeling of the material's behavior: the Johnson–Cook model

The material model used in all the simulations is Johnson–Cook's generic model. The material deforms plastically with the stress deviator associated with the flow. The integration of the constitutive relation is carried out using the radial recovery technique. The strain hardening of the material is a function of the logarithm of the equivalent plastic strain rate and of a certain power of the temperature:

$$\sigma_Y=(A+Bp^{\mathrm{N}})(1+C\,\mathrm{Log}\left[\frac{\dot{p}}{\dot{p}_0}\right])\left[1.-(\frac{T-T_0}{T_{\mathrm{melt}}-T_0})^{\mathrm{M}}\right] \tag{9}$$

where p denotes the accumulated plastic strain and T the temperature. This model has eight material parameters: A, B, C, N, M, $\dot{p}_0$ (the reference strain rate), T_0 (the reference temperature) and T_{melt} (the melting point in K). Adiabatic heating was assumed because the impact phenomena being considered are very fast and there is not enough time for heat conduction to take place during the simulation. We chose to convert 90% of the variation in plastic work into an increase in temperature. This ratio is commonly chosen because a portion of the plastic work is consumed in mechanisms other than temperature increase, but other ratios can be used. Thus, this model enables thermal softening to occur in the case of large plastic strains. Moreover, the choice of the high thermal conversion rate lowers the minimal "gluing" velocity.

2.3. Modeling of frictionless contact using Lagrange multipliers

Contact is taken into account by means of the Lagrange multiplier technique. When two surfaces come in contact, a contact energy term is added to the energy of the system. Let S_{contact} be the contact surface and λ_{contact} be the associated surface loads over the contact interface, and let V_{n_1} and V_{n_2} be the normal velocities of the two colliding objects. The expression of the contact energy is:

$$W_{\text{contact}} = \int_{S_{\text{contact}}} \underline{\lambda_{\text{contact}}}^{\mathrm{T}} (\underline{V_{n_1}} - \underline{V_{n_2}}) \, \mathrm{d}S \tag{10}$$

This equation is to be discretized based on the SPH points located on the external surfaces of the objects, which consist simply of series of SPH points. With this very simple approach, contact between surfaces boil down to contact between points. The approach simplifies into the detection of contacts among lists of points. When the distance between two SPH nodes belonging to the external surfaces becomes very small, then contact is said to occur between the surfaces, and a Lagrange multiplier is added to prevent them from getting closer in the direction defined by the positions of the points being considered.

2.4. Detection of contact using the pinball technique

The implementation of this very simple approach relies on the "pinball" method [18], which consists in surrounding each material point at which contact is likely to occur by a small sphere whose radius is chosen automatically so that the external surfaces of the two objects are completely covered, leaving no "holes". Contact is detected simply based on the interpenetration of the candidate spheres.

2.5. The adhesion model

The model which is proposed here was inspired by the "cohesive zone models" used in the static modeling of adhesion or in the modeling of crack behavior. These models are based on the use of a stress-gap curve relating the interaction force between the parts in contact to the opening of that same contact, as presented in [19,20]. Thus, one uses an adhesion energy (as in the Griffith model) along with a cohesive stress (as in the Barenblatt model [21]). In this section, we describe the chosen adhesion model and its implementation in the case of SPH methods associated with pinballs. This model produces forces that prevent the opening of the gap until a certain adhesion energy has been consumed. These forces are activated only if the gap between the two points considered tends to increase, and their magnitudes can be bounded if desired.

2.5.1. The mechanical models

As in fracture mechanics, the adhesion energy is characterized by a surface adhesion energy denoted G_{C}. The Griffith model consists in keeping the link active as long as the energy which is dissipated in opening the contact remains less than $G_{\mathrm{C}} S_{\text{adhes}}$ (where S_{adhes} is the adhesion surface between the two points in contact). For a pair of SPH points in contact with radii R_1 and R_2 respectively, this adhesion surface is determined by Eq. (11):

$$S_{\text{adhes}} = \frac{\pi}{2}(R_1^2 + R_2^2) \tag{11}$$

The Barenblatt model introduces a cohesive stress σ_c, which is active only during opening. In this case, there is an associated critical opening gap_c beyond which the cohesive forces cease to be active. These three quantities are related according to the following equation:

$$G_{\mathrm{C}} = \sigma_c \, gap_c \tag{12}$$

2.5.2. Modeling of the cohesive forces

The cohesive forces are determined in the same manner as in the case of contacts: one defines an additional load which prevents both of the points considered from moving.

These two points are associated with a Lagrange multiplier Λ which opposes the opening movement. The magnitude of the Lagrange multiplier is calculated as in the contact case: let us note that it is not bounded. Then, one calculates the work of this multiplier while the gap opens.

At each time step, the variation of the gap Δ_{gap} is known because, in explicit dynamics, the positions at the end of the time step are known at the onset. Thus, the work increment of the multiplier due to the opening of the gap between steps n and $n+1$ is:

$$\Delta W_{\text{adhes}} = \frac{1}{2}(\Lambda^n + \Lambda^{n+1})\Delta_{\text{jeu}} \tag{13}$$

Thus, the contact remains active until the energy consumed in opening the gap at the time step (n) being considered $(W^n_{\text{adhes}} = \sum_1^n \Delta W_{\text{adhes}})$ reaches the available cohesive energy $(G_{\mathrm{C}} S_{\text{adhes}})$.

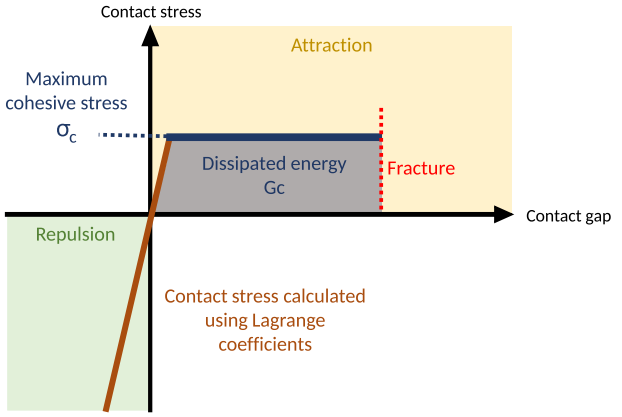

Fig. 2. The interaction law used in this study.

2.5.3. Limitation of the cohesive stress

One introduces the cohesive stress σ_C of magnitude Λ/S_{adhes}. Thus, the Dugdale–Barenblatt type of model used enables one to limit the maximum value of the cohesive stress in the contact zone. For each pair of interacting nodes, this leads to the definition of a stress-gap curve with a plateau which is similar to that of the Dugdale interaction model [19]. The use of Lagrange multipliers defined as in the previous section corresponds more to a Dirac model of the JKR type [20]. Thus, the cohesive stress model introduces a form of contact "softening" in dynamics.

2.5.4. Discussion of the adhesion model

Thus, the model can include a limit on the cohesive stress, which is a switch from a single-parameter model to a two-parameter model. If one does not limit the magnitude of the surface cohesive stress, that stress can become so high that it causes the materials on both sides of the interface to plastify. This drawback can be eliminated by setting a maximum cohesive stress. In any case, the model requires a knowledge of the surface over which the cohesion is in effect. In the case of an SPH calculation, this surface S_{adhes} is difficult to estimate accurately if the interfaces are highly distorted, which may be a problem for very-high-velocity impacts. An illustration of the model implemented for each pair of interacting nodes is given in Fig. 2, which shows the three stages of the behavior: a repulsion part for a negative gap, which is handled by the usual contact algorithm using Lagrange multipliers, an attraction part for a positive gap, in which Lagrange multipliers are first used as in the repulsion case, and an attraction part with a plateau when the stress associated with these Lagrange multipliers becomes greater than the maximum cohesive stress of the model.

The work of the adhesive stresses is accumulated for each pair of nodes which stick during the impact, leading to separation when the energy consumed in gap opening becomes greater than G_C.

3. Validation of the developments in the case of the elastic rebound of a cylinder impacting another cylinder

Here, we undertake to validate the cohesive model for simple cases and to compare the various possible parameter choices.

3.1. The elementary problem and its quasi-analytic solution

First, let us consider the very simple case of the impact of a rigid sphere of mass M projected vertically downward with a negative velocity V_0 onto another rigid sphere of mass m, initially at rest, supported by a spring of stiffness k (Fig. 3).

In the case of a spring with zero stiffness, one has simply two masses in contact. We shall show that in this case, and in this case alone, the final velocities of the spheres depend only on the cohesive energy G_C, and not on the magnitude of the cohesive load F_c that exists during the adhesion phase. The velocities after the rebound can be easily calculated by expressing the conservation of the momentum and kinetic energy through the impact. The velocities of masses M and m immediately after the impact are:

$$V_1 = \frac{M-m}{M+m}V_0$$
$$v_1 = \frac{2M}{M+m}V_0 \tag{14}$$

Immediately after the impact, the gap opens with the opening velocity $-V_0$. One can calculate the movement of the two masses by solving the momentum conservation equation for each mass. Let (A, V, U) and (a, v, u) be the acceleration,

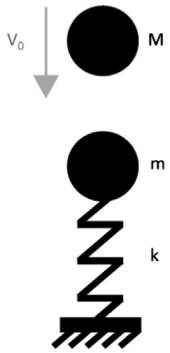

Fig. 3. The basic impact model.

velocity and displacement of masses M and m, respectively, and let F_c be the cohesive force that resists the movement. If $V_1 > 0$, one has:

$$\begin{aligned} M\,A &= -F_c \\ m\,a &= F_c \end{aligned} \tag{15}$$

which leads to the equations of the velocities and displacements of the two masses as functions of time:

$$\begin{aligned} V(t) &= V_0\frac{M-m}{M+m} - \frac{F_c}{M}t \\ v(t) &= V_0\frac{2M}{M+m} + \frac{F_c}{m}t \end{aligned} \tag{16}$$

$$\begin{aligned} U(t) &= V_0\frac{M-m}{M+m}\,t - \frac{F_c}{M}\frac{t^2}{2} \\ u(t) &= V_0\frac{2M}{M+m}\,t + \frac{F_c}{m}\frac{t^2}{2} \end{aligned} \tag{17}$$

Then, one can calculate the evolution of the gap over time. The cohesive forces cease to be active when the gap reaches the value gap_c. Thus, one can calculate the time at which the gap opens, which is the solution of the second-degree equation:

$$0.5\frac{F_c^2}{2}\frac{m+M}{m\,M}t^2 + V_0F_ct + G_C = 0 \tag{18}$$

The initial velocity must be sufficient for the mass to separate ($V_0 > \sqrt{2{\cdot}G_C\frac{m+M}{m\,M}}$). This separation occurs at time:

$$t_c = \frac{-V_0 + \sqrt{V_0^2 - 2{\cdot}G_C\frac{m+M}{m\,M}}}{F_c\frac{m+M}{m\,M}} \tag{19}$$

One can immediately see, by substituting t_c for t in Eq. (16), that the final velocities of the masses depend only on G_C. Now, if one considers that mass m is supported by a spring of stiffness k, Eq. (15) becomes:

$$\begin{aligned} M\,A &= -F_c \\ m\,a + ku &= F_c \end{aligned} \tag{20}$$

The evolution of the gap as a function of time in the absence of cohesive forces is given by the following equation:

$$gap(t) = V_1\,t - \frac{v_1}{\omega}\sin(\omega\,t) - F_c\left(\frac{1}{M} + \frac{1-\cos(\omega\,t)}{k}\right)\frac{t^2}{2} \tag{21}$$

with $\omega = \sqrt{\frac{k}{m}}$. There is no simple solution giving the time of separation, but one can solve the equation numerically (e.g., using Mathematica) for specific values of the constants. Table 1 compares, for a particular case, the separation velocities of mass M obtained with several values of F_c for the same cohesive energy G_C. Here, we chose a mass M equal to 1, a mass m equal to 2 and a stiffness k equal to 0 or 0.5. The initial velocity was -1. We chose $G_C = 0.2$. One can observe that the separation velocity of mass M is independent of the choice of F_c if $k = 0$, but not if $k = 0.5$.

Table 1
The effect of the choice of the cohesive stress on the particle's rebound velocity: elastic rebound $G_C = 0.2$.

F_c	$k = 0.0$	$k = 0.5$
0.05	0.0898	0.000
0.5	0.0898	0.086
5	0.0898	0.091

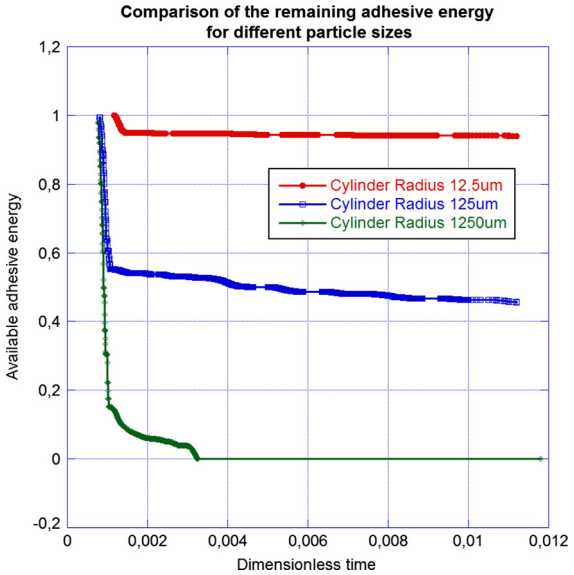

Fig. 4. The adhesion energy dissipation for the 12.5 µm, 125 µm and 1250 µm cylinders.

Thus, contrary to the quasi-static case, the choice of the magnitude of the cohesive stress has an essential influence on the rebound velocity when the elasticity of the bodies in contact is taken into account.

If ωt_c is small, one can carry out an expansion of the sine function in $gap(t_c)$, which leads to the same solution as when there is no elastic support. In this case, the magnitude of the cohesive force has no influence on the separation velocity of mass M.

3.2. The SPH model

In this section, our goal is to show that taking adhesion into account induces a size effect. This effect is predictable. The strain and kinetic energies are proportional to the volume, whereas the adhesion energy is proportional to the area. Consequently, if one does not take the adhesion effects into account, the cylinder's rebound effects are the same regardless of the size of the particle impacting the substrate. Conversely, if these forces are taken into account, the smaller the particles, the lower the rebound velocities.

3.3. Calculation results and comparison with the model

In this section, we first address the elastic impact of an aluminum cylinder of radius 12.5 µm and height 16.67 µm (so its initial kinetic energy is the same as that of a sphere of similar radius) which is projected at 20 $m{\cdot}s^{-1}$ onto a cylindrical target of radius 25 µm with the same height (16.67 µm). The cylindrical target is built-in at its base. The Young's modulus is 70 000 MPa, the Poisson's coefficient is 0.3 and the density is 2.7. We assumed a surface density of adhesion energy $G_C = 0.02$ $J{\cdot}m^{-2}$. The SPH mesh was compact hexagonal with 618 SPH in the impactor and 2526 SPH in the support. The radius of each SPH was 1.25 µm. Therefore, there were 20 SPH along a diameter. We chose not to set a maximum cohesive stress. The calculations were carried out with $7{\cdot}10^{-12}$ s time steps. Then, the same calculations were repeated after multiplying the time steps and the dimensions by 10, and then by 100, keeping the same material constants and the same adhesion surface energy. The calculations without and with adhesive forces were compared. The calculations without adhesive forces, which are dimensionless with respect to time, all lead to the same time history of the velocity of the impactor: in all cases, the particle rebounds with a velocity of 12 $m{\cdot}s^{-1}$. Fig. 4 shows the evolution of the total adhesion energy available in the contact for the three calculations. One can observe that the impact of the largest specimen quickly consumed all the available adhesion energy and the impactor bounced back. The two other cases show that only 5.5% (for

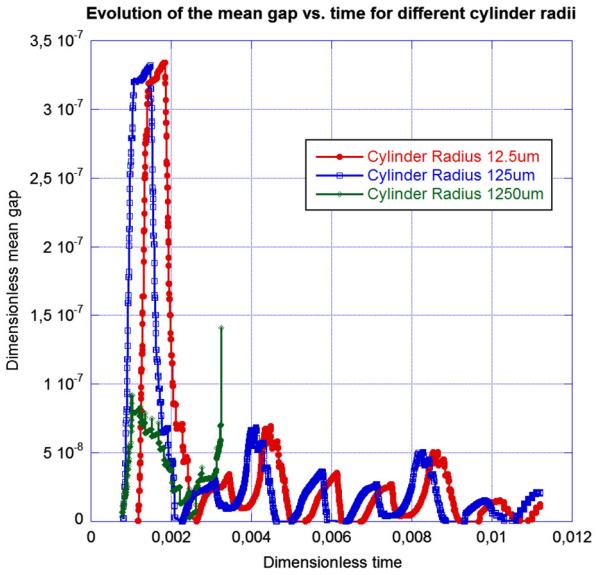

Fig. 5. Evolution of the gap for the 12.5 µm, 125 µm and 1250 µm cylinders.

the smallest particle) and 55% (for the medium-size particle) of the adhesion energy were consumed after 20 000 calculation steps. The two smallest particles remained stuck to the substrate. The observation of the time history of the average gap (Fig. 5) shows that after a first major rebound the gap oscillates and regresses progressively for the smallest two particles. These small oscillations about the motionless "stuck" state actually dissipate very little energy, which enables us to conclude that the sticking would continue even over longer calculations. For the largest specimen, the gap does not follow the same trend and tends toward infinity upon complete separation near $t = 3.5$ m s. The rebound velocity is much lower than in the free case (1.64 m·s^{-1} vs. 12 m·s^{-1}). As anticipated, there is, indeed, a size effect.

3.4. Discussion

We clearly showed the importance of scale effects in this problem. With the SPH model, we arrive at the same conclusions as with the quasi-analytic model: in the absence of adhesion, there is no scale effect. If there is adhesion, the smaller the particle, the better it adheres. It might seem surprising that the particle would stick even though the adhesion energy is very small compared to the initial kinetic energy. The observation of the time history of the energies of the various subsets shows that the two objects start vibrating at very high frequency during the contact. The activation of the cohesive forces leaves enough time for these high-frequency energy exchanges to take place and, thus, to borrow from the initial kinetic energy.

Fig. 6 shows the evolution of the various energies involved during the impact, with and without adhesion, for the largest-diameter cylinder and for the intermediate-diameter cylinder. One can see that the main difference between the larger cylinder which separates and the smaller cylinder which sticks lies in the distribution of the strain energy (internal energy) between the substrate and the particle. The longer sticking time in the case of the medium-sized cylinder allows more strain energy to move from the particle to the substrate, which hampers the separation of the particle.

4. Impact of a spherical projectile onto a substrate

Now, let us consider the impact of a spherical particle of radius 12.5 µm onto a parallelepipedic substrate of length 75 µm and height 33.4 µm. The particle and the substrate were meshed using respectively 737 and 15 776 SPH. First, we will study an elastic impact and focus on the effect of the choice of the adhesion model's maximum cohesive stress on the rebound velocity. Then, we will study how the boundary condition chosen at the base of the substrate affects the rebound. Finally, we will address the elastic–plastic case, which gives a more realistic representation of the behavior of the particle's and substrate's material, using the Johnson–Cook elastic–plastic model with adiabatic thermal softening.

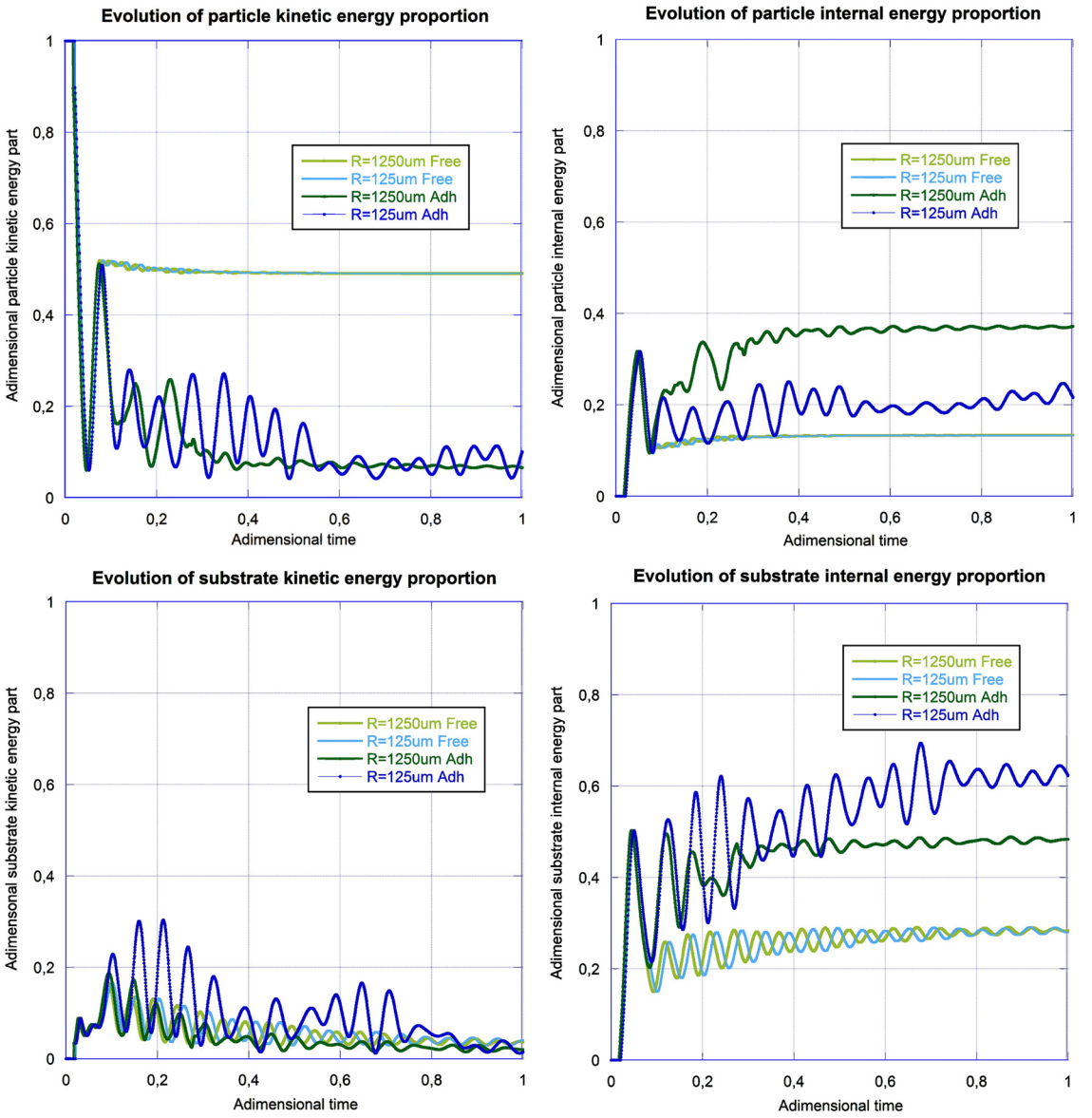

Fig. 6. Energy distribution during the cylinder impacts.

4.1. Impact in elasticity: effect of the adhesion model

Here, we compare the results of the rebound velocities with various adhesion parameters for a -20 m·s^{-1} velocity of the spherical impactor. The adhesion surface energy is still $G_C = 0.02$ J·m^{-2}. First, let the parallelepiped be built-in at its base. The Griffith adhesion model uses the Lagrange coefficient given by the contact algorithm directly. The Dugdale model requires a maximum cohesive stress σ_c, whose magnitude was incremented from 100 to 1600 MPa. Because of this choice, the largest allowable gap prior to the rupture of a cohesive link was 0.2 nm, which remains very small compared to the size of the objects being considered and the radius of the SPH spheres. Fig. 7 shows the variation of the particle's velocity during impact as a function of the maximum adhesive stress. One can see that the choice of the maximum adhesive stress has a significant influence on the time history of the velocities, and that the final rebound velocity is highly dependent on the adhesive stress level chosen (Fig. 8).

When the maximum cohesive stress increases, the rebound velocity decreases to reach a stable value of 30% of the initial velocity. The irregularities between 800 and 1300 MPa are due to the occurrence of additional rebounds in the impact history due to an increase in the cohesive recovery load on the particle. The calculation was carried out in elastoplasticity by multiplying the initial yield stress of the material by 1000. This result is important because it proves that for a dynamic

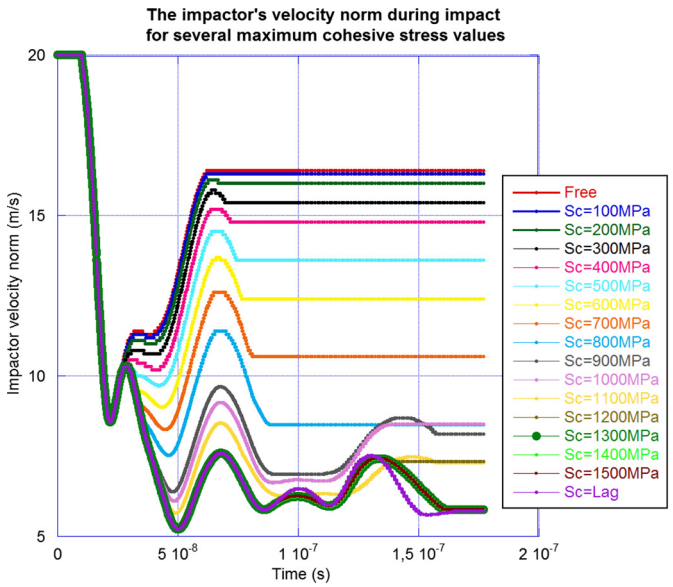

Fig. 7. Evolution of the velocity norm during impact for several values of the maximum cohesive stress.

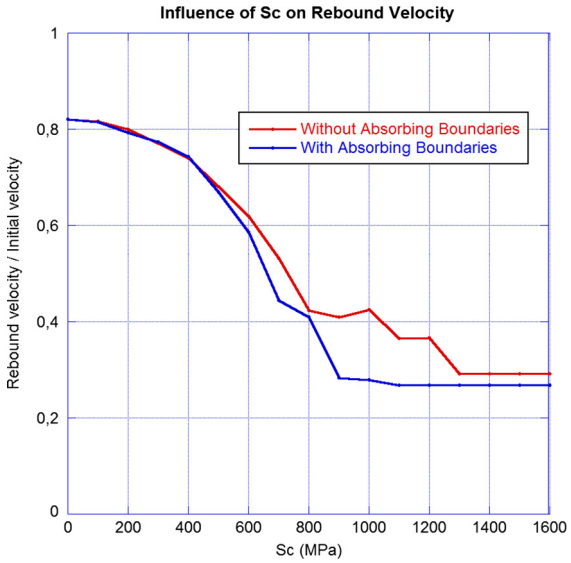

Fig. 8. Evolution of the rebound velocity norm during impact for several values of the maximum cohesive stress.

impact, contrary to the static case, the choice of the plateau stress of the cohesive model is significant. This influence will be even greater in the plastic case.

4.2. Impact in elasticity: effect of the modeling of the substrate's absorbing boundaries

Next, absorbing boundaries were added to the model in order to simulate a semi-infinite substrate. An elastic impedance was applied over the bottom and the vertical sides of the parallelepipedic substrate. At each SPH node of the boundary, the impedance condition can be expressed as:

$$\mathbf{F_{SPH}} = -\mathbf{V}\sqrt{\rho\, E}\, S_{\mathrm{SPH}} \tag{22}$$

This is a force which is directed opposite to the point's velocity and is proportional to that velocity and to the square root of the product E ρ.

Fig. 8 shows the influence of these absorbing boundaries on the rebound velocity as a function of the maximum adhesive stress σ_c. One can observe a decrease in the rebound velocity compared to the case without absorbing boundaries. This difference increases as the value of σ_c increases until, again, it reaches a plateau.

Table 2
The Johnson–Cook material parameters for aluminum.

Parameter	Value	Unit
A	148.4	MPa
B	345.5	MPa
N	0.183	
C	0.001	
$\dot{p}_0$	1	s^{-1}
M	0.9	
T_0	300	K
T_{melt}	916	K

Table 3
The effect of G_C on the percentage of stuck SPH in the absence of a maximum cohesive stress.

Impact velocity ($m{\cdot}s^{-1}$)	G_C							
	0.002	0.01	0.015	0.017	0.018	0.019	0.020	0.05
100	0%	0%	0%	0%	0%	0%	0%	5%
200	0%	0%	0%	0%	0%	0%	0%	19%
300	0%	0%	0%	0%	0%	0%	0%	19%
400	0%	0%	0%	4%	1%	7%	12%	47%
500	0%	0%	1%	1%	3%	3%	6%	37%
600	0%	1%	6%	14%	19%	20%	24%	51%
700	0%	0%	0%	0%	0%	0%	0%	48%
800	0%	0%	0%	0%	0%	9%	9%	40%
900	0%	11%	21%	21%	21%	22%	22%	36%
1000	18%	23%	31%	31%	31%	31%	31%	38%

Thus, as anticipated, the presence of these boundaries results in an energy loss in the system leading to a slight decrease in the rebound velocity and a change in impact behavior (in terms of the number of rebounds prior to separation), which should facilitate the adhesion of the particles.

The two cases presented here (built-in substrate and semi-infinite substrate) are the bounds of the actual case of a substrate whose size is finite, but usually much greater than the size of the particle.

4.3. Impact in the case of material nonlinearities

Here, we address a more realistic impact model which takes into account the elastic–plastic behavior of the material, which is represented by a Johnson–Cook law (Eq. (9)). The parameters chosen to represent the behavior of aluminum were taken from the literature and are given in Table 2. The specific heat was set at 904 $J{\cdot}kg^{-1}{\cdot}K^{-1}$.

Experiments have shown that for particles of a given diameter adhesion occurs only in a specific velocity range (typically 400 to 700 $m{\cdot}s^{-1}$ for an Al–Al impact). Therefore, our objective is to reproduce this observation numerically. The cohesion energy is unknown. Let us try, through calculations, to identify a value of the adhesion energy which matches the experimental observation, and then to study the influence of the associated cohesive stress. Here, we present, for several values of the impact velocity between 100 and 1000 $m{\cdot}s^{-1}$, the results of a series of calculations of the cohesive energy G_C and of the cohesive stress σ_c. The calculations were carried out with a fixed maximum time step equal to $7{\cdot}10^{-12}$ s.

4.4. Effect of the impact velocity in the elastic–plastic case

First, let us consider the calculations in which no limit was set on the cohesive stress and we allowed the adhesion energy G_C to vary. It is relatively difficult to tell what really happened in the calculations because they always stopped after a certain simulation time (typically, 5000 time steps). In general, the transfers of energy among the particle, the substrate and the infinite medium had not been completed, although the adhesion energy was practically stable. Besides, this consumed adhesion energy represented only a very small portion of the initial kinetic energy. Therefore, it is very difficult to distinguish between rebound or sticking based on energy balances and a comparison between the particle's kinetic energy and the unused adhesion energy. We chose to decide about adhesion based on the percentage of the nodes that stuck. Thus, we counted the number of nodes in the particle which were stuck at the end of the calculation and compared that number with the maximum number of nodes which were stuck during the calculation. This was used as the sticking criterion: we decided that if more than 1% of the nodes remained stuck at the end of the calculation that meant that the particle had stuck. Of course, this value is completely arbitrary and can be debated. The duration of the calculations was chosen in order to allow this number to become stable over a period equivalent to or double the transition period. Table 3 summarizes these results for a range of values of G_C between 0.002 and 0.05. The conclusion from this table is that if G_C is too high sticking occurs regardless of the impact velocity. Once G_C becomes equal to or less than 0.02, there

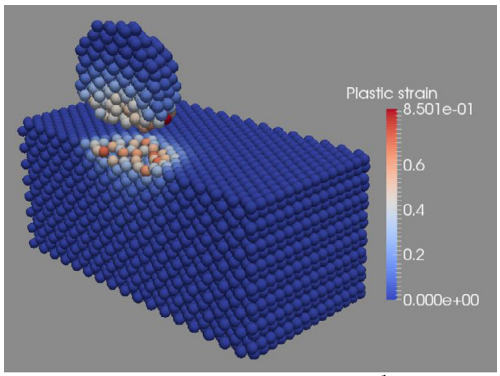

(a) Impact at 300 $m{\cdot}s^{-1}$

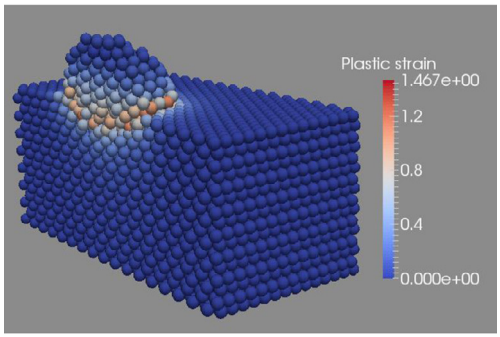

(b) Impact at 600 $m{\cdot}s^{-1}$

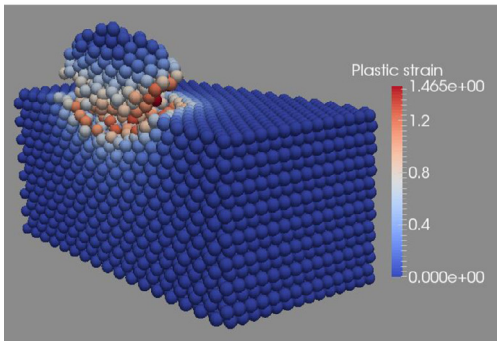

(c) Impact at 700 $m{\cdot}s^{-1}$

Fig. 9. The deformed bodies along with the accumulated plastic strains.

is no sticking if the impact velocity is small and sticking if the velocity is in a range which depends on the value of G_C. The minimum velocity is between 300 and 500 $m{\cdot}s^{-1}$. The particle bounces when the impact velocity exceeds 600 $m{\cdot}s^{-1}$. This result comes close to the experimental results for this type of aluminum/aluminum impact. The maximum plastic strains are in the order of 1.5. There is a second sticking range, associated with impact velocities greater than 900 $m{\cdot}s^{-1}$, which does not correspond to experimental observations. The accumulated plastic strains given by the calculations exceed 5 in the vicinity of the interfaces. At this strain level, damage most certainly occurs in the material and generates a third body, which prevents sticking. Therefore, these calculation results are not very realistic. Fig. 9 shows, for $G_C = 0.02$, the deformed shapes of the particle and the substrate along with the isovalues of the accumulated plastic strains for the three impact velocities (300, 600 and 700 $m{\cdot}s^{-1}$) at final simulated time (0.35 μs in every case). The faster the impact, the more the particle flattens out and penetrates the substrate. One can observe an accumulated plastic strain which culminates at 1.47 for a relatively coarse mesh. These strains are concentrated near the interfaces, which is a sign of significant shearing in these regions.

Fig. 10 shows, for the same cases, the isocurves of Von Mises' stresses. These stresses are quasi-uniform in the sphere and localized beneath the impact in the substrate. Fig. 11 shows the final temperatures for the case which corresponds to the highest velocity. The maximum temperature is almost 500 K. The particle does not melt.

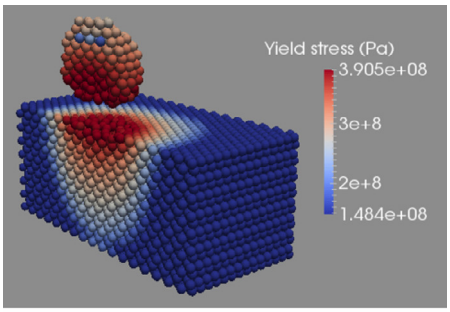

(a) Impact at 300 $\mathrm{m{\cdot}s^{-1}}$

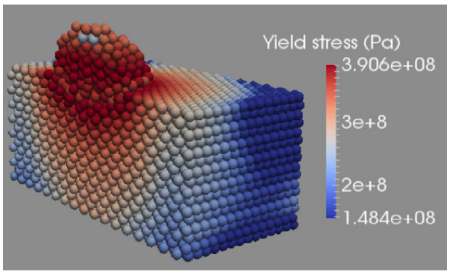

(b) Impact at 600 $\mathrm{m{\cdot}s^{-1}}$

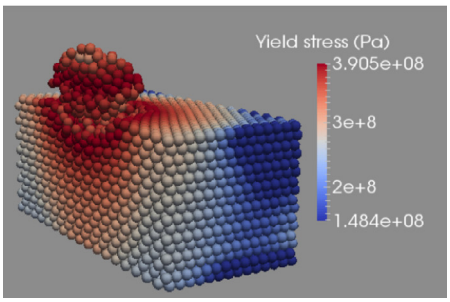

(c) Impact at 700 $\mathrm{m{\cdot}s^{-1}}$

Fig. 10. The deformed bodies along with the Von Mises stresses.

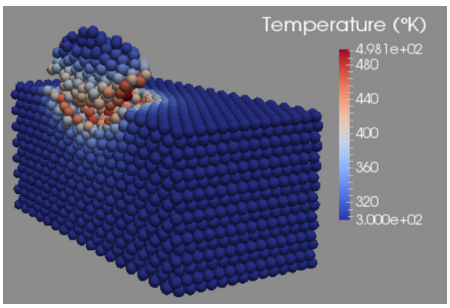

Fig. 11. The deformed bodies at 700 $\mathrm{m{\cdot}s^{-1}}$ along with the temperatures in K.

Finally, we studied the model with the addition of a maximum cohesive stress σ_c. The same calculations were carried out with stress values equal to 100, 200, 300 and 500 MPa. The results did not change significantly. The sticking velocity range is relatively unaffected by the value of σ_c.

4.5. Discussion

The adhesion energy alone is insufficient to assess what happens in dynamics when the material behavior is elastic. If one simulates plastic behavior, there is not much difference between the models with a maximum cohesive stress and those without if one is interested only in whether the particle sticks to its substrate or not. This is an interesting result because it makes setting the parameters of the problem easier. The proposed model is unrealistic when the impact velocities are

too high because it predicts sticking at very high impact velocities, which is not observed experimentally. This is due to an excessive flattening of the particle which leads to huge plastic strains. In such conditions, damage probably occurs in the material and generates a third body in the contact, which hampers sticking. This cannot be reproduced by the model proposed in this work. A Johnson–Cook damage model that will be able to describe the material fragmentation is being implemented to simulate the third body apparition. For very large strains, the error in the calculations of the sticking area for each point should also be taken into account and the method improved in order to achieve more physically realistic results at high speed.

5. Conclusions

In this paper, we presented a method for simulating the effect of adhesive forces on the rebound of particles projected onto a substrate at high speed. The models were implemented in a fast dynamics SPH code. We showed that size effects have an essential influence on sticking when the size of the particles is relatively small. In addition, the proposed model is capable of reproducing the experimental observation that sticking occurs only in a certain range of impact velocities. The simulation also predicts sticking at very high impact velocities ($> 1000\ \mathrm{m{\cdot}s^{-1}}$). This prediction is not very realistic because the plastic strains can then exceed 500% near the interfaces, even with the relatively coarse mesh chosen. The introduction of a maximum cohesive stress plays an important role when the rebound is elastic. The effect of this limit on the adhesive stress is less obvious in elastoplasticity. The type of model developed here will be used systematically to simulate sticking with all sorts of material pairs used for Cold Spray. The effect of alternative local sticking activation criteria (e.g., Shear Stress Instability/Adiabatic Shear Band) will also be studied. For that purpose the mesh will have to be refined to be able to represent the shear bands with enough details. This type of approach can also be used for fluid/structure adhesive forces in the case of very small sized problems.

Acknowledgement

Funding for this project was provided by a grant from the “Région Rhône-Alpes”.

References

[1] A. Papyrin, V. Kosarev, S. Klinkov, A. Alkimov, V. Fomin, Cold Spray Technology, Elsevier, Oxford, 2007.
[2] D. Gilmore, R. Dykhuizen, R. Neiser, T. Roemer, M. Smith, Particle velocity and deposition efficiency in the cold spray process, J. Therm. Spray Technol. 8 (4) (1999) 576–582, http://dx.doi.org/10.1361/105996399770350278.
[3] X.-T. Luo, C.-X. Li, F.-L. Shang, G.-J. Yang, Y.-Y. Wang, C.-J. Li, High velocity impact induced microstructure evolution during deposition of cold spray coatings: a review, Surf. Coat. Technol. 254 (2014) 11–20, http://dx.doi.org/10.1016/j.surfcoat.2014.06.006.
[4] H. Assadi, F. Grtner, T. Stoltenhoff, H. Kreye, Bonding mechanism in cold gas spraying, Acta Mater. 51 (15) (2003) 4379–4394, http://dx.doi.org/10.1016/S1359-6454(03)00274-X.
[5] W.-Y. Li, W. Gao, Some aspects on 3D numerical modeling of high velocity impact of particles in cold spraying by explicit finite element analysis, Appl. Surf. Sci. 255 (18) (2009) 7878–7892, http://dx.doi.org/10.1016/j.apsusc.2009.04.135.
[6] J. Xie, D. Nélias, H. Walter-Le Berre, K. Ogawa, Y. Ichikawa, Simulation of the cold spray particle deposition process, J. Tribol. 137 (4) (2015), http://dx.doi.org/10.1115/1.4030257.
[7] A. Manap, T. Okabe, K. Ogawa, Computer simulation of cold sprayed deposition using smoothed particle hydrodynamics, Proc. Eng. 10 (2011) 1145–1150, http://dx.doi.org/10.1016/j.proeng.2011.04.190.
[8] J. Xie, Phd thesis: simulation of cold spray particle deposition process, http://theses.insa-lyon.fr/publication/2014ISAL0044/these.pdf, 2014.
[9] W.-Y. Li, S. Yin, X.-F. Wang, Numerical investigations of the effect of oblique impact on particle deformation in cold spraying by the {SPH} method, Appl. Surf. Sci. 256 (12) (2010) 3725–3734, http://dx.doi.org/10.1016/j.apsusc.2010.01.014.
[10] V. Lemiale, P. King, M. Rudman, M. Prakash, P. Cleary, M. Jahedi, S. Gulizia, Temperature and strain rate effects in cold spray investigated by smoothed particle hydrodynamics, Surf. Coat. Technol. 254 (2014) 121–130, http://dx.doi.org/10.1016/j.surfcoat.2014.05.071.
[11] B. Yildirim, H. Fukanuma, T. Ando, A. Gouldstone, S. Müftü, A numerical investigation into cold spray bonding processes, J. Tribol. 137 (1) (2015) 011102.
[12] J.J. Monaghan, Smoothed particle hydrodynamics, Rep. Prog. Phys. 68 (8) (2005) 1703.
[13] R. Vignjevic, J. Campbell, Review of development of the smooth particle hydrodynamics (sph) method, in: S. Hiermaier (Ed.), Predictive Modeling of Dynamic Processes, Springer, US, 2009, pp. 367–396.
[14] M. Liu, G. Liu, Smoothed particle hydrodynamics (sph): an overview and recent developments, Arch. Comput. Methods Eng. 17 (1) (2010) 25–76, http://dx.doi.org/10.1007/s11831-010-9040-7.
[15] B. Maurel, A. Combescure, S. Potapov, A robust sph formulation for solids, Eur. J. Comput. Mech. 15 (5) (2006) 495–512, http://dx.doi.org/10.3166/remn.15.495-512.
[16] F. Caleyron, A. Combescure, V. Faucher, S. Potapov, {SPH} modeling of fluidsolid interaction for dynamic failure analysis of fluid-filled thin shells, J. Fluids Struct. 39 (2013) 126–153, http://dx.doi.org/10.1016/j.jfluidstructs.2013.02.023.
[17] B. Maurel, A. Combescure, An sph shell formulation for plasticity and fracture analysis in explicit dynamics, Int. J. Numer. Methods Eng. 76 (7) (2008) 949–971, http://dx.doi.org/10.1002/nme.2316.
[18] T. Belytschko, M.O. Neal, Contact-impact by the pinball algorithm with penalty and Lagrangian methods, Int. J. Numer. Methods Eng. 31 (3) (1991) 547–572, http://dx.doi.org/10.1002/nme.1620310309.
[19] N. Chandra, H. Li, C. Shet, H. Ghonem, Some issues in the application of cohesive zone models for metalceramic interfaces, Int. J. Solids Struct. 39 (10) (2002) 2827–2855, http://dx.doi.org/10.1016/S0020-7683(02)00149-X.
[20] U. Schwarz, A generalized analytical model for the elastic deformation of an adhesive contact between a sphere and a flat surface, J. Colloid Interface Sci. 261 (1) (2003) 99–106, http://dx.doi.org/10.1016/S0021-9797(03)00049-3.
[21] J. Willis, A comparison of the fracture criteria of Griffith and Barenblatt, J. Mech. Phys. Solids 15 (3) (1967) 151–162, http://dx.doi.org/10.1016/0022-5096(67)90029-4.